Nanoscale

PAPER

View Article Online
View Journal

Cite this: DOI: 10.1039/d5nr04652a

Engineering tip-to-tip cubic assemblies of octahedral nanoparticles for enhanced generation of near-field electromagnetic hot spots

Qiang Zhao, †[a] SeHyun Park, †[b] Soohyun Lee,[a] Kyuvin Hur,[b] Lichun Liu *[c] and Sungho Park *[b]

Engineering unique architectures at the nanoparticle and colloidal scales represents a promising strategy for harnessing physicochemical interparticle interactions, particularly to enhance near-field light focusing. Although electric fields tend to concentrate at regions of high curvature, such as sharp tips, the presence of the latter features alone does not substantially strengthen the near-field enhancement. Instead, directly assembling two sharp tips in a tip-to-tip configuration represents an effective way to maximize near-field focusing by generating highly localized electromagnetic "hot spots". To achieve this goal, we introduce an innovative approach for obtaining a tip-to-tip assembly of octahedral nanoparticles. This strategy involves encapsulating solid octahedral nanoparticles within cubic shells, serving as structural building blocks, to form point contacts between the flat surfaces of the cubic shell and the sharp tips of the octahedron. By arranging these distinctive structures in a serial configuration, we achieve a controlled tip-to-tip alignment. Within this architecture, the inner tips induce charge concentration on the flat planes, while the serial arrangement further enhances near-field focusing across adjacent building blocks. This configuration exhibits distinct near-field characteristics compared to assemblies composed of simple solid cubes or isolated octahedral nanoparticles, thus providing a novel strategy for optimizing near-field interactions in nanoscale systems.

Received 4th November 2025,
Accepted 19th January 2026

DOI: 10.1039/d5nr04652a

rsc.li/nanoscale

Introduction

Surface-enhanced Raman scattering (SERS) is a powerful spectroscopic technique with significant potential, owing to its unique ability to identify analyte molecules with characteristic fingerprint information without destroying the sample.[1–6] Moreover, the electric field[7–12] plays a crucial role in SERS applications, which dramatically enhances the Raman intensity of analyte molecules.[13,14] Recently, engineering nanoparticle architectures has emerged as a promising strategy for enhancing the electric field by creating inter- and intra-particle gaps.[15–21] Among various nanostructures,[22–25] complex nanoframe structures have been extensively studied and demonstrated excellent detection limits due to their high density of electromagnetic hot spots. However, these architectures typically exhibit weaker SERS signals compared to solid nanoparticles in practical applications.[26] Besides, sharp-tipped architectures, such as octahedral nanoparticles,[27,28] are especially effective at concentrating electric fields at their vertices. However, while individual sharp tips can produce a local electric field enhancement, their overall near-field focusing ability remains limited without precise spatial organization. To regularly organize these nanoparticles with sharp tips provides one potential solution to overcome the barrier of the low SERS intensity in practical applications that complex nanoframe structures suffer. Notably, recent studies have confirmed the feasibility of precisely engineered tip-to-tip configurations between adjacent nanoparticles, which effectively generate intense electromagnetic 'hot spots' and significantly amplify near-field intensity.[29] While this approach provides a viable solution to overcome the limitations of conventional sharp-tipped architectures, the systematic and programmable organization of such tip-to-tip architectures remains insufficiently explored in current research.

Herein, we present a strategy for achieving the tip-to-tip assembly of Au octahedra in cubic shells (AOICSs), serving as building blocks with unique surface charge accumulation. We systematically investigated the effect of the key parameter – the

[a]Department of Chemistry, Sungkyunkwan University (SKKU), Suwon 16419, Republic of Korea
[b]Department of Chemistry, Yonsei University, Seoul 03722, Republic of Korea. E-mail: sparknano@yonsei.ac.kr
[c]College of Biological, Chemical Sciences and Engineering, Jiaxing University, Jiaxing, Zhejiang Province, 314001, P. R. China. E-mail: lichun.liu@zjxu.edu.cn
† These authors contributed equally to this work.

shell thickness – and the results reveal that an optimal shell thickness of ~5 nm maximizes the surface charge accumulation, whereas a thickness of 14 nm suppresses it entirely. Notably, while tip-to-tip superposition was evident in dimer configurations, a considerable enhancement of the SERS signal was observed in these structures, owing to charge accumulation superposition between two AOICSs controlled by the degree of mismatch (DM), which played a critical role. By building serial assemblies of these unique structures, we achieved a controlled tip-to-tip configuration that enhanced near-field focusing across adjacent units with a low degree of mismatch. As a result, the tip-to-tip assembly exhibited considerable signal increase compared to conventional Au nanocubes, as evidenced by the detection of three types of analytes including 2-naphthalenethiol (2-NTT), rhodamine 6G (R6G) and tetramethylthiuram disulfide (Thiram), and real-time detection of three types of chemical warfare gas (4 seconds for 2-chloroethyl phenyl sulfide (2-CEPS), 6 seconds for 2-chloroethyl ethyl sulfide (2-CEES) and 2-chloroethyl methyl sulfide (2-CEMS)), highlighting the distinct advantage provided by the present superposition architecture.

Results and discussion

As illustrated in Fig. 1, cubic tip-to-tip superstructures were prepared by employing AOICSs as building blocks. The AOICSs were synthesized through a rationally designed two-step procedure, involving (1) an Ag-mediated morphological transformation of gold octahedra into cubic structures, and (2) a galvanic replacement reaction that converted the solid cubes to hollow shells with a central embedded octahedron. Initially, gold octahedral nanoparticles (Au Oh NPs) with well-defined sharp tips were selected as starting materials. Then, silver was

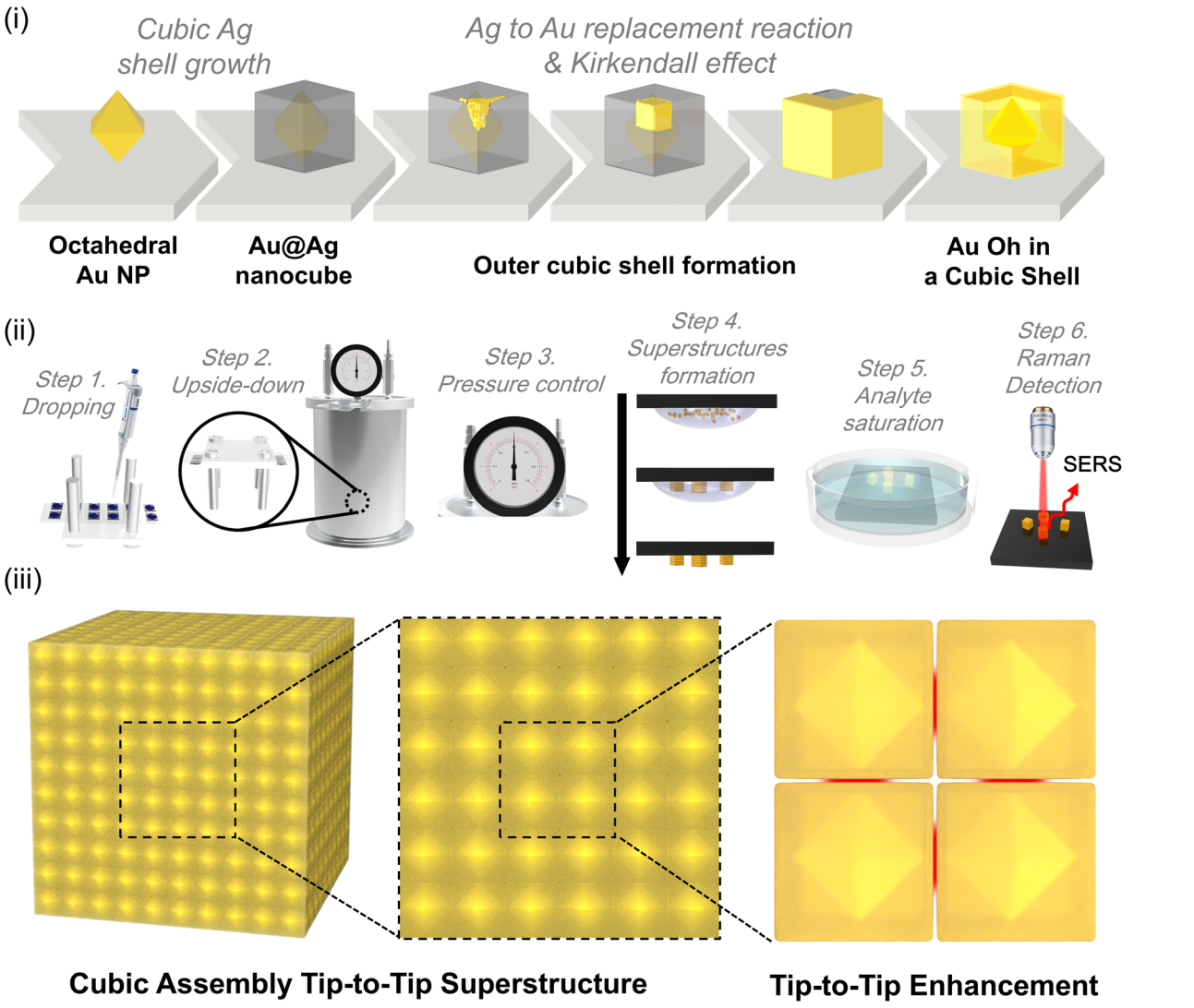

Fig. 1 Schematic illustration of the synthesis of Au-octahedra-in-cube-shells (AOICSs) and preparation of the cubic-assembled tip-to-tip superstructure.

preferentially deposited on the {111} facets of the Au Oh NPs, resulting in the formation of an Ag cube encapsulating a gold octahedral core. The introduction of Au^{3+} ions initiated a galvanic replacement reaction (Au^{3+} + 3Ag → $3Ag^{+}$ + Au), which directed the morphological evolution toward the final AOICSs, characterized by a central Au octahedron enclosed within a hollow cubic shell. The fabrication and characterization of cubic assembly-mediated tip-to-tip superstructures, adapted from our previous work,[30] involved six key steps. 1. Dispersion and deposition: high-concentration AOICSs dispersed in 5 mM hexadecyltrimethylammonium chloride (CTAC) were drop-cast onto silicon substrates. 2. Inverted assembly: the substrate was inverted and secured within a Teflon cell. 3. Pressure-assisted packing: the Teflon cell was placed in a an N_2 chamber at 3 bar to promote dense and uniform packing through slow solvent evaporation. 4. Superstructure formation and cleaning: controlled evaporation under optimized surfactant conditions enabled the formation of long-range ordered superstructures. Residual CTAC was subsequently removed by treatment with 10 mM $NaBH_4$ to expose clean Au surfaces. 5. Analyte adsorption: the assembled tip-to-tip superstructures were immersed in analyte solutions of varying concentrations to facilitate molecular adsorption. 6. SERS measurements: SERS signals were directly measured utilizing the intense localized electromagnetic fields at the tip-to-tip junctions within the superstructures for signal amplification under 785 nm extinction.

Fig. 2A–C displays representative field-emission scanning electron microscopy (FE-SEM) images of the intermediate nanostructures, illustrating their high uniformity in both size and morphology throughout the synthesis process. As shown in Fig. 2A, the initial Au octahedra exhibited an average edge length of 82 ± 3 nm. Upon Ag deposition, the particles transformed into cubic structures with an increased edge length of 116 ± 5 nm (Fig. 2B). Following the galvanic replacement reaction, the resulting hollow shell structures were clearly visible in the SEM images, with Fig. 2C and the corresponding inset highlighting the thin-wall thickness of the final AOICSs. Notably, the reaction kinetics were precisely controlled by adjusting the concentration of Au^{3+} ions, which proved critical for the formation of well-defined AOICSs (Fig. S1). Meanwhile, X-ray diffraction (XRD) analysis revealed the crystallographic evolution from Au octahedra to Au@Ag nanocubes and finally to AOICSs. The initial exclusive Au {111} facet dominance (2θ = 38.32°) of Au octahedra transitioned to a mixed phase upon Ag deposition, characterized by an obvious intensity reduction and slight peak shift (2θ = 38.24°), and the emergence of distinct Ag {200} reflections (2θ = 44.44°). Subsequent galvanic removal of Ag in AOICSs increased the Au {111} intensity and a peak shift to the right (2θ = 38.30°) due to the removal of most silver, and the Ag {200} facet changed to the Au {200} facet (2θ = 44.52°). Compositional analysis using high-resolution transmission electron microscopy (HR-TEM) and energy-dispersive X-ray spectroscopy (EDS) mapping confirmed the successful synthesis of the AOICSs, revealing Au and Ag atomic percentages of 68.51% and 31.49%, respectively (Fig. 2D). The corresponding elemental scan along the red line in Fig. 2D, shown

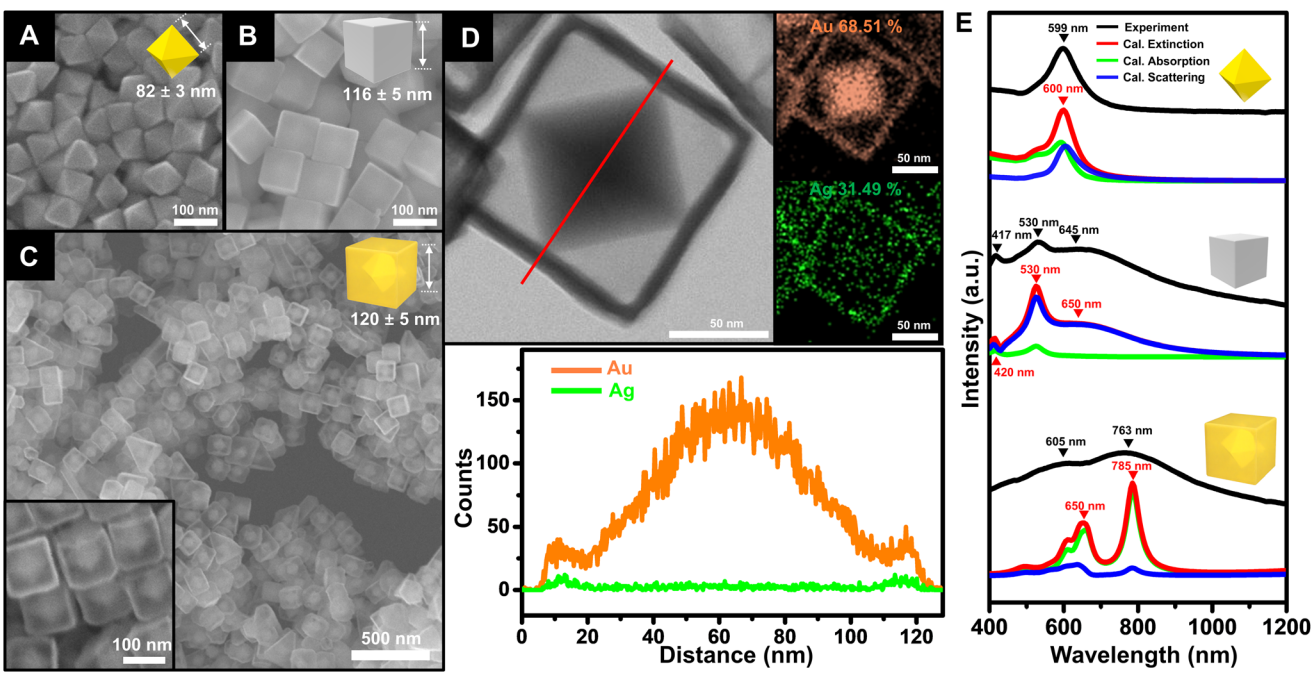

Fig. 2 (A–C) FE-SEM images of Au Oh NPs, Au@Ag nanocubes, and AOICSs showing the structural evolution from Au Oh NPs to AOICSs through a two-step process of regulated Ag deposition and successive galvanic exchange. (D) TEM image and corresponding elemental mapping and line-scanning plot of AOICSs, showing Au (orange color) and Ag (green color) compositions. (E) Corresponding FEM-simulated and experimental vis-NIR spectra.

in the image below, indicates that the structure was predominantly composed of Au, with trace amounts of Ag uniformly distributed throughout the shell. The central position of the octahedral core was further confirmed by TEM images of AOICSs acquired at different angles (5°, 15°, 25°, and 45°), as shown in Fig. S3. The octahedral core remained centered at all viewing angles, indicating a well-defined central configuration, which is attributed to the mild galvanic replacement method. The structural evolution was further validated by visible-near-infrared (vis-NIR) spectroscopy. The Au octahedra (edge length: 82 ± 3 nm) exhibited a distinct localized surface plasmon resonance (LSPR) peak centered at 599 nm shown in the top section of Fig. 2E. The corresponding optical spectra calculated by the finite element method (FEM) are shown below the experimental trace, with extinction (red line), absorption (green line), and scattering (blue line) components clearly delineated. The dominant spectral feature at ~600 nm corresponded to the dipolar plasmon mode (Fig. S4). After Ag overgrowth, the edge length increased to 116 ± 5 nm, and three distinct peaks appeared at 417, 530, and 645 nm. These features were consistent with the FEM theoretical simulations, which exhibited corresponding peaks at 420, 530, and 650 nm (represented by the red line in the middle section of Fig. 2E). The above peaks were attributed to different plasmonic modes, as shown by FEM simulations (Fig. S5), *i.e.*, dipole (~650 nm), quadrupole (~530 nm), and higher-order multipole (~420 nm) modes. Notably, the induced charge separation on the central Au octahedral core generated an opposite mirror charge on the

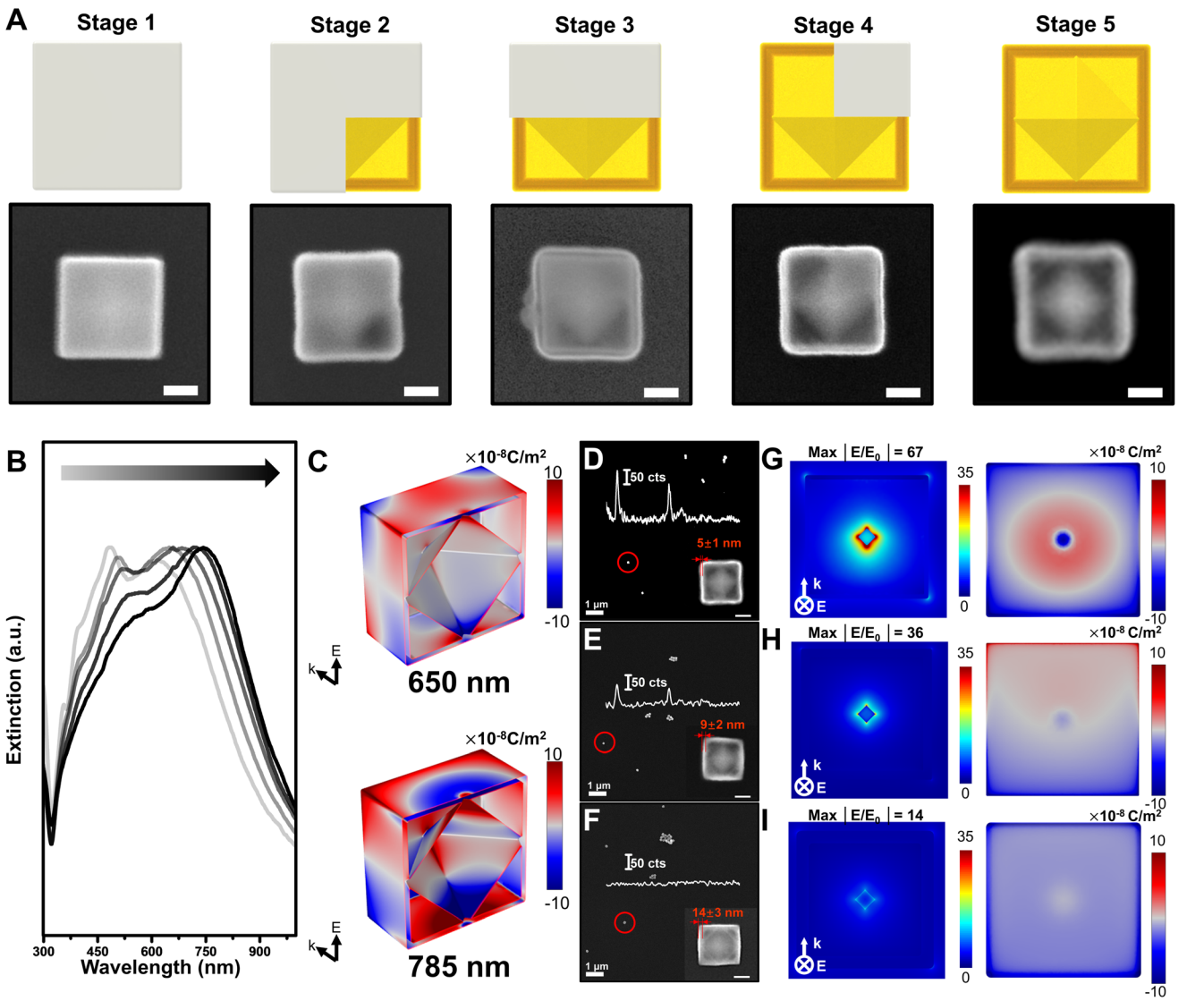

Fig. 3 (A) FE-SEM images and (B) corresponding UV-vis-NIR spectra of the galvanic replacement reaction of Au@Ag nanocubes at different intermediate stages. (C) FEM-simulated surface charge distribution of AOICSs at 650 and 785 nm extinction. (D–F) FE-SEM images of single particles with different outer shell thickness used for spSERS measurements of 2-naphthalenethiol (2-NTT) at a concentration of 10^{-3} M under a 785 nm laser, with corresponding spSERS spectra (Raman shift: 1000–1800 cm^{-1}). (G–I) FEM calculations (cross-section: the junction between inner Au octahedron and outer cubic shell) corresponding to (D–F). Scale bars = 50 nm.

surrounding Ag shell, significantly influencing the observed plasmonic behavior.

To gain deeper insight into the galvanic replacement process, the intermediate stages were systematically monitored (Fig. 3). The observation revealed that the reaction between Ag and Au^{3+} proceeded *via* the Kirkendall effect, characterized by the initial formation of voids at the cube corners. The progression of the galvanic replacement reaction was divided into five stages, defined by the extent of Ag hollowing, as evidenced by the increasing cavity size surrounding the Au octahedron core. These voids gradually expanded into larger cavities as the reaction proceeded, ultimately resulting in the complete removal of silver (Fig. 3A). Notably, the transformation did not occur uniformly in all directions but rather followed a corner-initiated pathway. This anisotropic evolution is consistent with previous results.[31] The progression of the galvanic replacement reaction was further confirmed by vis-NIR spectroscopy (Fig. 3B). The characteristic peaks of Ag nanocubes at 353 and 417 nm became gradually weaker, while new peaks emerged at 530 and 648 nm, corresponding to the evolving bimetallic nanostructures. As the reaction proceeded, these peaks exhibited a pronounced red shift from 648 to 660 and 723 nm, eventually reaching 763 nm, reflecting the gradual transformation into hollow Au-based architectures with altered dielectric environments and plasmonic coupling characteristics. The simulated optical spectra of the AOICSs, shown in the bottom section of Fig. 2E, display two prominent peaks at 650 and 785 nm. The corresponding charge distributions at these wavelengths are illustrated in Fig. 3C. A relatively moderate charge separation was observed at 650 nm, with mild accumulation on the faces and corners of the cubic shell. In contrast, at 785 nm, the charge localization became significantly more pronounced. In particular, strong electron accumulation was observed at the vertices of the central Au octahedron, accompanied by corresponding mirror charges on the flat facets of the surrounding cubic shell, especially concentrated at the contact points between the inner octahedral tips and the outer cubic shell surfaces. This enhanced charge localization highlights the plasmonic coupling at the tip-to-face junctions, which is critical for the observed field enhancement.

Notably, as we described above (Fig. S5 and Fig. 3C), the outer cubic shell and inner octahedral core exhibited opposite charge distributions, which will cause the offset of opposite charges, determined by the thickness of the outer cubic shell. When the thickness of the cubic shell is around 5 nm, the outer shell has quite a limited amount of charge on the surface (Fig. S8). Meanwhile, facing sufficient mirror charges provided by the inner core octahedron, the offset of opposite charge is not obvious. FEM simulation analysis revealed that the distinct surface charge separation in the AOICSs led to a remarkably high enhancement of the local electric field and apparent surface charge accumulation (Fig. 3G). When the thickness of the shell increased from 5 to 9 nm, the offset of opposite charges became more severe. As the simulations showed, the degree of surface charge accumulation was gradually reduced (Fig. 3H and I). Overall, as the shell thickness increases, the total charge within the system rises proportionally. This enhanced charge accumulation shifts the dominant influence on the surface charge distribution from the inner regions to the outer shell. Due to its larger surface area and greater charge capacity, the outer shell exerts a stronger electrostatic screening effect, redistributing the electric field in a manner that suppresses further charge buildup at the surface. This is accompanied by a corresponding decrease in electric field enhancement ($|E/E_0|$), dropping from 67 to 36 and 14, respectively. These trends were supported by single-particle SERS (spSERS) measurements using 2-naphthalenethiol as a Raman probe under the extinction of a 785 nm laser, which confirmed that the surface charge accumulation effect became negligible when the shell thickness exceeded ~9 nm, likely due to limited charge penetration (insets of Fig. 3D–F). Notably, the accuracy and precision of our AOICS calculations have been rigorously validated through a mesh-control study. As shown in Fig. S9A, the simulated electric field (E-field) distribution patterns remain virtually identical across different mesh densities, demonstrating the high precision and robustness of our computational model. However, a detailed quantitative analysis revealed that the fractional part of the local field enhancement factor ($|E/E_0|$) exhibited non-negligible fluctuations under varying mesh resolutions (Fig. S9B). To ensure the reliability of our calculation, we only adopted the integer part of the calculated maximum $|E/E_0|$ values, which will be used for subsequent analysis. This practice effectively eliminates the uncertainty associated with the less reliable decimal places, thereby guaranteeing the solid validity of our key conclusions regarding field enhancement performance. In comparison, Au nanocubes lacking the internal voids exhibited no detectable spSERS signals, owing to their weak electric fields, as shown in Fig. S6 ($|E/E_0| = 11$). Notably, a thinner wall produced a significantly stronger electric field enhancement, reminiscent of the "nanotrench effect" described in a previous study.[32] In contrast, complete removal of the outer cubic shell or inner octahedron (retaining only the Au octahedron or Au cubic shell) resulted in negligible spSERS signals (Fig. S7 and S8, respectively), emphasizing the critical synergy between outer shells and inner octahedral structures in plasmonic enhancement.

To investigate the near-field enhancement mediated by charge accumulation on the planar surfaces of the AOICSs, we hypothesized that, if the charge separation occurred on the inner shell faces (induced by the presence of the Au octahedron within the hollow cavity), then the face-to-face alignment of two closely packed AOICSs would induce a strong interparticle plasmonic coupling. This interaction would be expected to generate highly localized electromagnetic hot spots at the interface between the facing planes. Furthermore, we assumed that the intensity of these hot spots would be sensitive to the degree of alignment between opposite faces, with deviations from perfect face-to-face matching resulting in a reduced field enhancement. To test this hypothesis, AOICSs were dispersed onto a silicon substrate, and AOICS dimers with varying degrees of face alignment mismatch were identi-

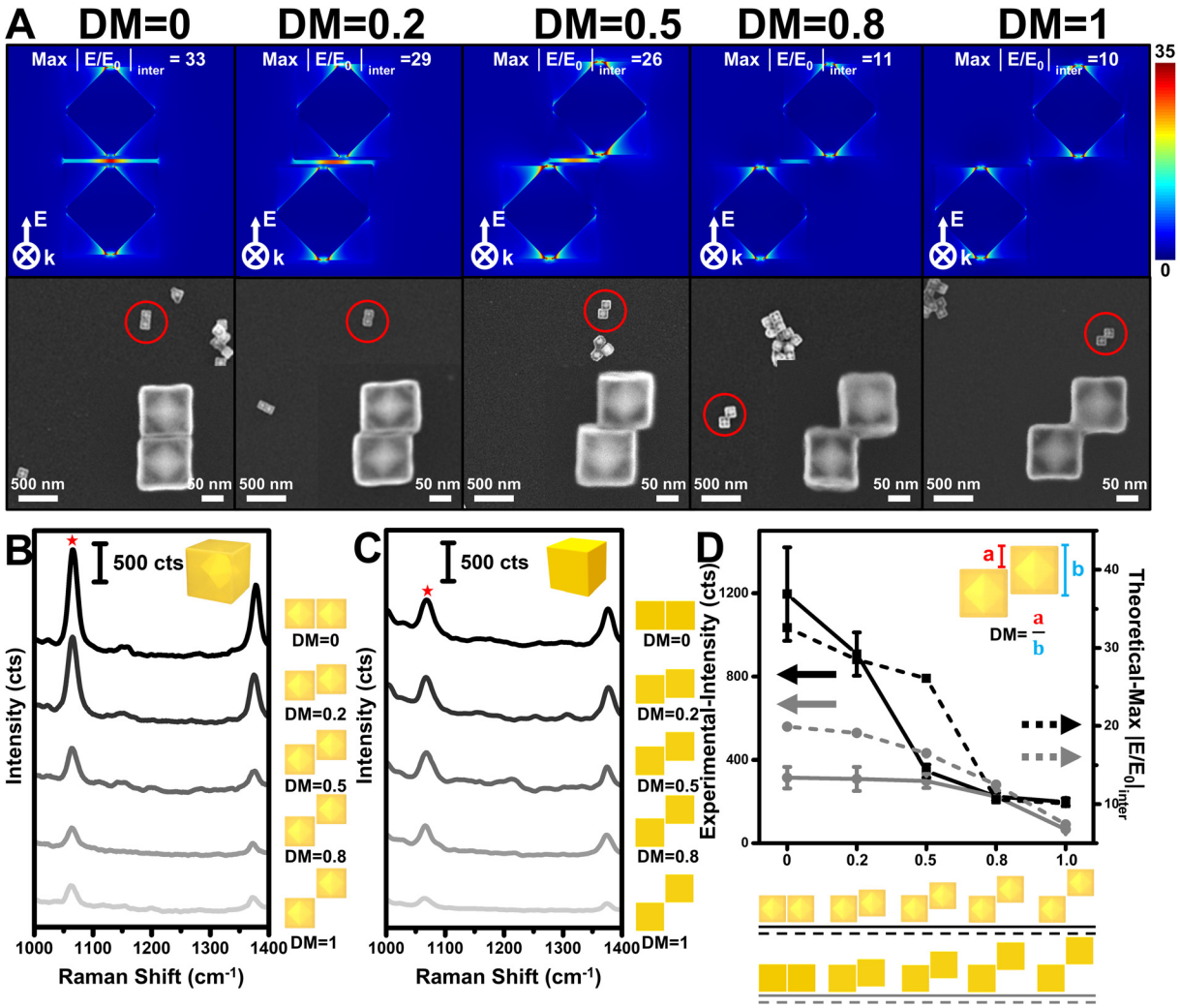

Fig. 4 (A) FE-SEM images and simulated electric field enhancement (cross-section: the middle plane of dimer structures) of AOICS dimers with different degrees of mismatch (degree of mismatch (DM) = 0, 0.2, 0.5, 0.8, 1). (B and C) Experimental SERS spectra of AOICS and Au nanocube dimers with different degrees of mismatch (Raman probe: 2-NTT (10^{-3} M), laser wavelength: 785 nm). (D) Scatter plot illustrating the relationship between dimer SERS intensity at 1064 cm^{-1} and degree of mismatch (AOICS and Au nanocube dimers), with their corresponding value of simulated electric field enhancement. The asterisk marks in panels (B) and (C) indicate the SERS peak intensity used for panel (D).

fied, as shown in the representative SEM images in Fig. 4A. The DM between adjacent AOICS dimers was quantitatively defined as the ratio a/b, where a represents the length of the non-contacted (misaligned) region between the opposite faces of two adjacent dimers, and b denotes the total edge length of a single planar face. In the case of perfect face-to-face alignment, $a = 0$, resulting in DM = 0. Conversely, in a complete misalignment scenario, $a = b$, yielding the maximum DM value of 1. This parameter thus provides a quantitative measure of the structural deviation from the ideal coupling geometry, which is critical for precisely controlling the alignment to optimize the plasmonic hot spot intensity. As illustrated by the theoretical simulations in Fig. 4A, when two AOICSs with 4 ± 1 nm gap distance were perfectly aligned (DM = 0), the contact points between the inner Au octahedra and the outer cubic shells lay along the same central axis, optimizing the geometric overlap and maximizing the electric field enhancement ($|E/E_0|_{inter}$ = 33) within the interparticle gap. However, as the degree of misalignment increased (DM = 0.2, 0.5, 0.8, and 1), the tip-to-tip coupling was progressively disrupted, leading to a systematic decrease in electric field enhancement, with corresponding $|E/E_0|_{inter}$ values of 29, 26, 11, and 10, respectively. These results highlight the critical importance of a precise geometric alignment for achieving strong near-field coupling and hot spot generation. The corresponding SERS measurements using 2-NTT as a Raman probe under 785 nm laser for each AOICS dimer configuration with 4 ± 1 nm are presented in Fig. 4B, which shows that the SERS intensities varied consistently with the DM value, in agreement with the theoretical predictions. As a control experiment, we performed similar simulations and SERS measurements using dimers composed of pure-Au cubes. In this case, the near-field

enhancement was notably weaker than that observed for the AOICS dimers, and the decrease in field intensity with increasing DM was more gradual. Consistently, the SERS peak intensities of the Au cube dimers exhibited only a mild decline as DM increased from 0 to 1. Fig. 4D and S10 show a summary of the SERS intensity profiles and corresponding electromagnetic field enhancement values as a function of DM. The experimental peak intensities at 1064 cm^{-1} (left-hand *y*-axis) for the AOICSs and pure Au cubes are shown using dark and grey solid lines, respectively. Correspondingly, the theoretical max$|E/E_0|$ values (right-hand *y*-axis) are represented by dark and grey dashed lines for AOICSs and pure Au cubes, respectively. Notably, a critical transition point for the AOICSs was observed around DM ~0.5, before which the SERS intensities displayed a sharp drop. This inflection indicates that once the tip-to-tip alignment is sufficiently disrupted, the plasmonic coupling efficiency is significantly reduced. Beyond this threshold, the SERS intensities reached a plateau, suggesting that only a weak peripheral coupling occurred between the misaligned cube faces, where the inner octahedral tips were no longer spatially engaged (*i.e.*, DM values from *ca.* 0.5 to 1.0), Notably, all the experiments were conducted under a fixed incident polarization condition. This setup can lead to certain discrepancies; for instance, the DM = 1 dimer, which was theoretically expected to generate intense localized fields at the interparticle nanogap, exhibited an unexpectedly weak SERS enhancement. This outcome is attributable to the suboptimal coupling of the fixed polarization with its dominant plasmonic mode, but it does not represent the investigative priority of this work. Given that our core research scope is dedicated to probing the mechanism of geometrically guided tip-to-face coupling and its supremacy in local field enhancement for SERS, the DM = 1 case will not be subjected to further detailed analysis. This plateau-like behavior mirrors the response observed in pure Au cubes, where central charge accumulation is absent (Fig. S11, bottom image). Further charge distribution simulations confirmed that the intense SERS signals in the AOICSs arise from strong charge accumulation at the tip-to-shell junctions between the embedded Au octahedron and the cubic shell (Fig. S11, top image). These findings emphasize the critical role of geometrically guided tip-to-face coupling in enhancing local electromagnetic fields and optimizing the SERS performance.

While our dimer SERS measurements clearly demonstrated the correlation between degree of mismatch and signal intensity, another crucial factor, the interparticle contact area, must also be taken into account when evaluating field enhancements within the inter-nanogap region. To further confirm that the near-field focusing is predominantly induced by the embedded Au octahedral core, we conducted SERS measurements on isolated AOICS trimers with distinct spatial arrangements. Two configurations were investigated: (1) a linear (single-column) alignment, designed to maximize tip-to-tip superposition along a continuous axis, thereby promoting coherent charge accumulation and plasmonic coupling; and (2) a split (two-column) alignment, which spatially disrupts the coherence of charge accumulation while preserving the same total interparticle contact area as in the linear configuration. This comparative analysis isolates the role of the geometric charge coherence from the effect of the contact area in determining the strength of the near-field enhancement. Simulations revealed a clear difference between the two configurations: the linear trimer arrangement (Fig. 5A) exhibited a significantly enhanced electric field ($|E/E_0|$ = 105), attributed to the cumulative effect of tip-to-tip superposition along aligned octahedral–cubic contact points. This coherent alignment facilitated effective plasmonic coupling and concentrated near-field localization across the trimer axis. In contrast, the split configuration (Fig. 5B) exhibited a markedly lower electric field enhancement ($|E/E_0|$ = 61), as the spatial separation between particles disrupted the coherence of charge accumulation. This reduction occurred even though the configurations maintained equivalent interparticle contact areas, highlighting the critical role of the geometric alignment and charge continuity in achieving optimal near-field enhancement. The experimental SERS measurements closely mirrored the simulation results: linear AOICS trimers produced an average of 2067 counts, approximately 1.5 times higher than the 1359 counts recorded for the split trimers. In contrast, control experiments using Au nanocube trimers (Fig. S12) showed no significant variation in SERS intensity between the two configurations, confirming that the enhanced signals in the AOICS assembly arise specifically from tip-to-tip alignment-driven plasmonic coupling enabled by the embedded octahedral cores. While the overall length of the AOICS trimer could, in principle, contribute to an antenna-like resonance effect, the fact that no enhancement occurs in the gold cube trimer control—which has the same overall size but a different internal structure—rules out global dimensions as the main contributing mechanism and this conclusion is validated by FEM simulation (Fig. S13), which demonstrates that the electric field enhancement attributable solely to the overall dimensions is negligible. The observed enhancement is therefore governed primarily by the superposition of surface charge accumulation existing in the AOICSs.

Having gained a clear understanding of the role of core-induced surface charge accumulation in near-field focusing, we extended this principle to bulk SERS measurements by arranging AOICSs into cubic close-packed superstructures. The well-defined outer cubic geometry of the AOICSs facilitates their spontaneous self-assembly into ordered arrays under controlled solvent evaporation, achieving uniform and reproducible interparticle spacing and alignment, which led to a large-area near-field enhancement.

As illustrated in Fig. 1, AOICSs were assembled into long-range-ordered microscopic superstructures, forming macroscopic powders. It is worth emphasizing again that the formation of the macroscopic superstructures followed a precisely controlled evaporation-induced self-assembly process, with cetyltrimethylammonium chloride (CTAC) acting as a critical structure-directing agent, where its bilayer adsorbed on the crystal facets promoted face-to-face alignment. Concurrently,

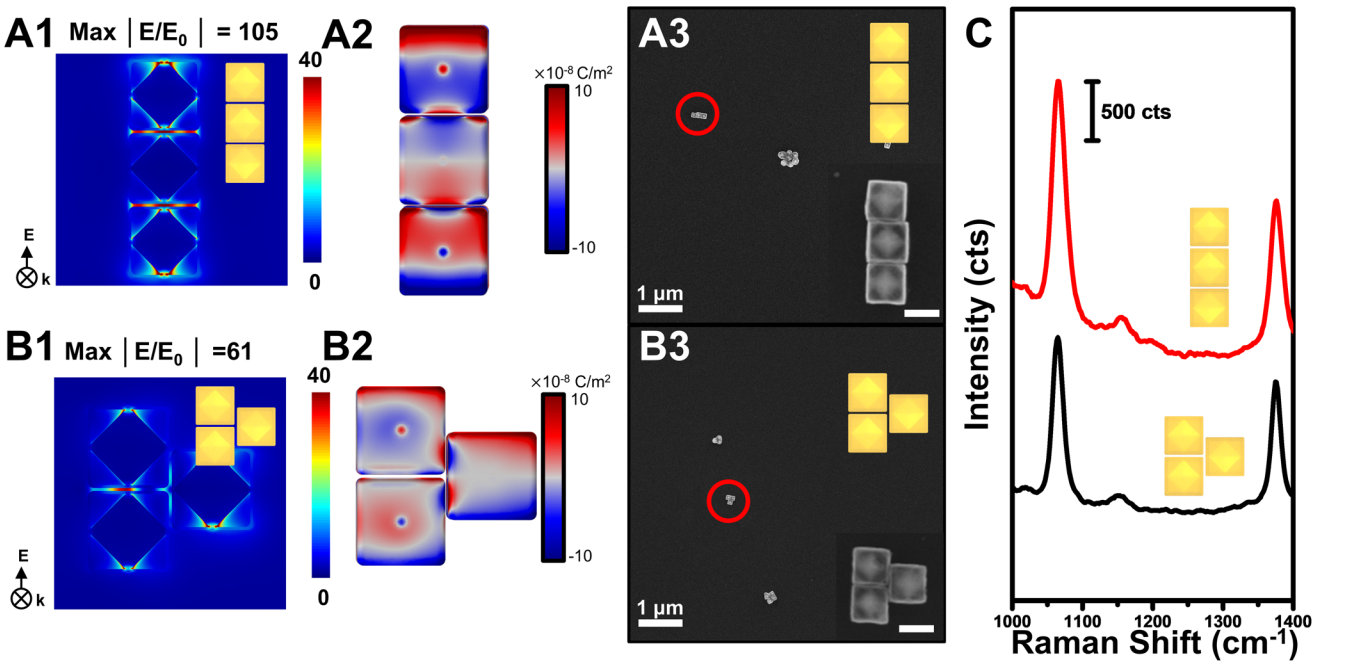

Fig. 5 (A and B) FE-SEM images and simulation of electric field enhancement (cross-section: the middle plane of trimer structures) and surface charge distribution of AOICS trimers with linear and split alignment, and (C) corresponding trimer SERS spectra using 2-NTT at a concentration of 10^{-3} M under a 785 nm laser. Scale bars = 100 nm.

the slowed evaporation kinetics provided by the high pressure allowed sufficient time for the AOICSs to diffuse, rotate, and settle into their thermodynamically most stable configuration—namely, the low-DM, tip-to-tip alignment. This synergistic protocol ensures the reproducible fabrication of large-area, highly ordered superstructures essential for consistent macroscopic SERS performance. The corresponding SEM images (Fig. 6A and Fig. S14) systematically illustrate the progression of the assembly process, highlighting the exceptional uniformity in both the overall powder morphology and the individual AOICS building blocks. Notably, the tip-to-tip alignments of the AOICSs discussed above were retained within the assembly, extending in all three spatial dimensions (x, y, and z); this resulted in a highly ordered three-dimensional plasmonic lattice, ensuring optimal tip-to-tip superposition and a high density of plasmonic hot spots (as described within the dashed lines in Fig. 6A). Meanwhile, this approach was also extended to Au nanocubes as a comparison group (Fig. S15). To systematically evaluate the universality of the high-density plasmonic hot spots in AOICS superstructures, three analytes with distinct chemical structures and properties were investigated: (1) 2-naphthalenethiol (2-NTT), a toxic compound associated with acute toxicity, skin/eye irritation, and potential central nervous system effects, commonly used in chemical engineering; (2) rhodamine 6G (R6G), a synthetic dye with potential carcinogenicity, skin/eye/respiratory irritation, and aquatic toxicity; and (3) tetramethylthiuram disulfide (Thiram), a fungicide widely applied in agriculture and industry, presenting potential liver and embryonic toxicity. AOICS superstructures delivered significantly stronger SERS signals for all three analytes compared with Au nanocube superstructures (Fig. 6B and C), confirming their universal enhancement effect. It is worth noting that the plasmonic contribution of the silver component present in our AOICS structures (Ag = 31.49%, Fig. 2D) cannot be ignored. To specifically evaluate the role of silver, we performed a control experiment using Au@Ag core–shell nanocubes that possess a similar Ag percentage (Ag = 26.3%) shown in Fig. S16A but which lack the intricate AOICS superstructure. As shown in Fig. S16B and D, while the presence of Ag in these control structures led to a moderate SERS enhancement for the three analytes tested (2-NTT, R6G and Thiram), their performance was consistently and significantly lower than that of the AOICS superstructures. This result decisively demonstrates that the extraordinary SERS enhancement reported here is primarily governed by the unique geometry and plasmonic coupling within the AOICS superstructure, rather than merely by the silver residue. Therefore, the comparison with pure Au nanocubes serves as a conservative reference point, which is more broadly representative. Additionally, taking 2-NTT as an example, the AOICS superstructures also exhibited excellent signal reproducibility with a relative standard deviation (RSD) of 2.5% for the 1064 cm^{-1} peak intensity under 785 nm (4 mW) laser excitation over 600 s (Fig. S17). Furthermore, the substrate showed high environmental stability; over 86.5% of the initial signal intensity was retained after seven days of ambient air exposure (Fig. S18). This charge-driven hot spot mechanism also improved the detection limits of the three analytes (Fig. S19–S21), by one order of magnitude for 2-NTT and R6G and two orders of magnitude for Thiram, compared with Au nanocube

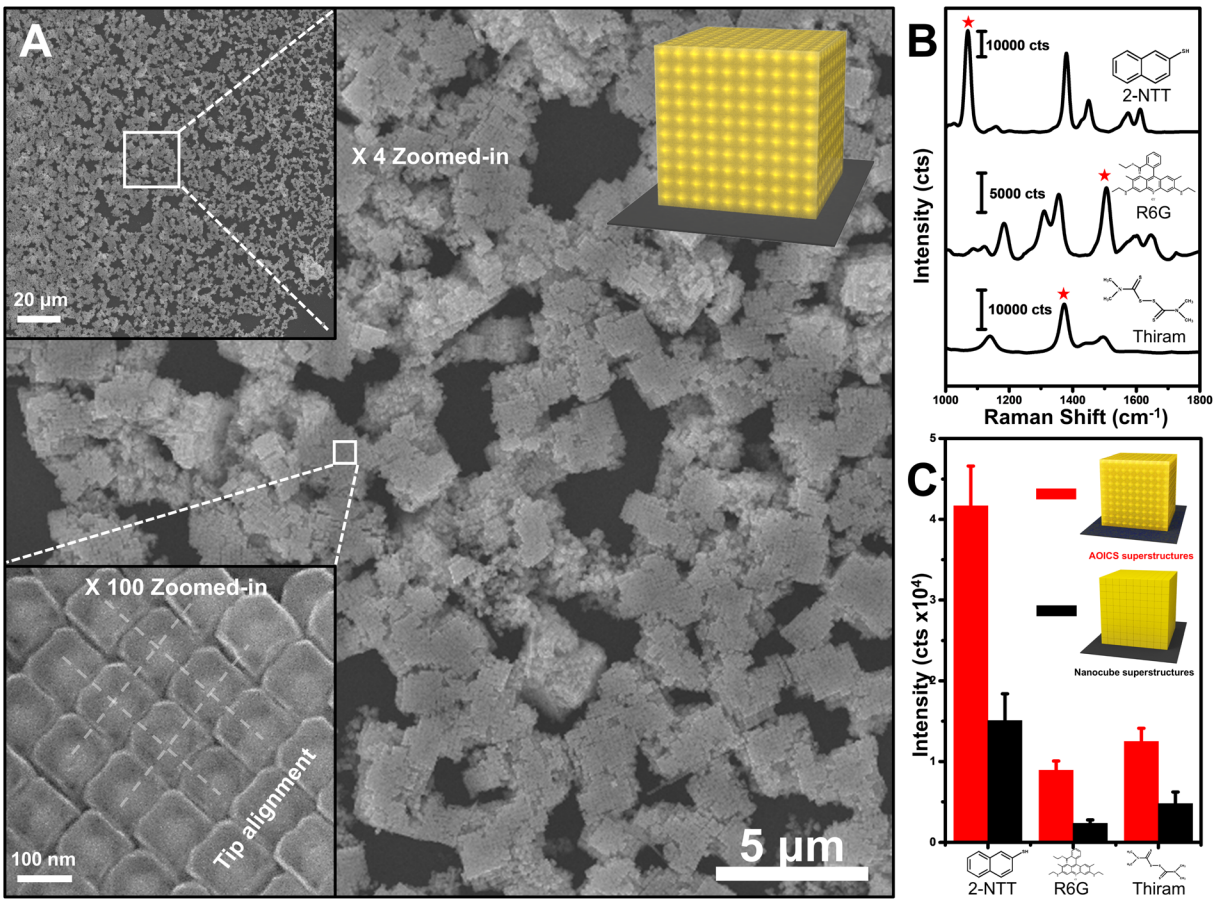

Fig. 6 (A) FE-SEM images of AOICS superstructures from low to high magnifications. (B) SERS spectra of 2-NTT, R6G, and Thiram, and (C) SERS peak intensity comparison of two superstructures composed of Au nanocubes (black bars) and AOICSs (red bars) used in bulk SERS measurements. The intensity of 2-NTT, R6G, and Thiram was measured from 1064, 1506, and 1373 cm^{-1} at a concentration of 10^{-5} M under a 785 nm laser, respectively. The asterisk marks in panel (B) indicate the SERS peak used for quantification of SERS peak intensities in panel (C).

superstructures. Noticeably, bulk SERS measurements with the three analytes as probes revealed two key features: (i) peak intensity saturation occurred above 10^{-5} M, where the cubic face centers were fully covered by analyte molecules, contributing to the signal; (ii) as the concentration decreased below this level, incomplete coverage of the octahedral–cubic contact points caused a sharp drop in intensity, which stabilized at concentrations below 10^{-7} M. In contrast, the Au nanocube superstructures showed a linear decrease across the entire concentration range, indicating the absence of charge accumulation at the cubic face centers and highlighting the critical role of charge-driven hot spot formation in AOICS superstructures.

Recently, with increasingly tense and turbulent international situations and the increasing concern over potential threats from chemical warfare agents (CWAs), rapid and accurate detection has become essential to minimize exposure to toxic gases to ensure human physical health. To assess the performance of the AOICS superstructures in CWA detection, a calibration gas generator was employed to produce CWA simulant vapors with tunable concentrations by adjusting the number of permeation tubes and the operating temperature (Fig. 7A). The generated gases were directed through a detection chamber containing the substrate, enabling analyte adsorption and real-time Raman monitoring. Three mustard gas simulants were examined: 2-chloroethyl phenyl sulfide (2-CEPS), 2-chloroethyl ethyl sulfide (2-CEES), and 2-chloroethyl methyl sulfide (2-CEMS). For 2-CEPS, AOICS superstructures provided detectable Raman signals within 4 s at 1 ppm, supported by heat maps and real-time spectra (Fig. 7B and C). In contrast, Au nanocube superstructures required 28 s under identical conditions, a sevenfold slower response (Fig. S22A and B). For CEES and CEMS, AOICS superstructures achieved clear signals within 6 s (Raman shift: 628 cm^{-1} and 750 cm^{-1} for CEES, 626 cm^{-1} for CEMS), demonstrating the strong charge-driven hot spot effect confirmed by heat maps and Raman spectra. (Fig. 7D–G). In comparison, Au nanocube superstructures failed to generate effective signals at 10 ppm due to weak field enhancement (Fig. S22C–F). The observed fast gas-phase response is enabled by a surface-layer sensing mechanism. During the short time of gas flow (~4–6 s), the analyte gas

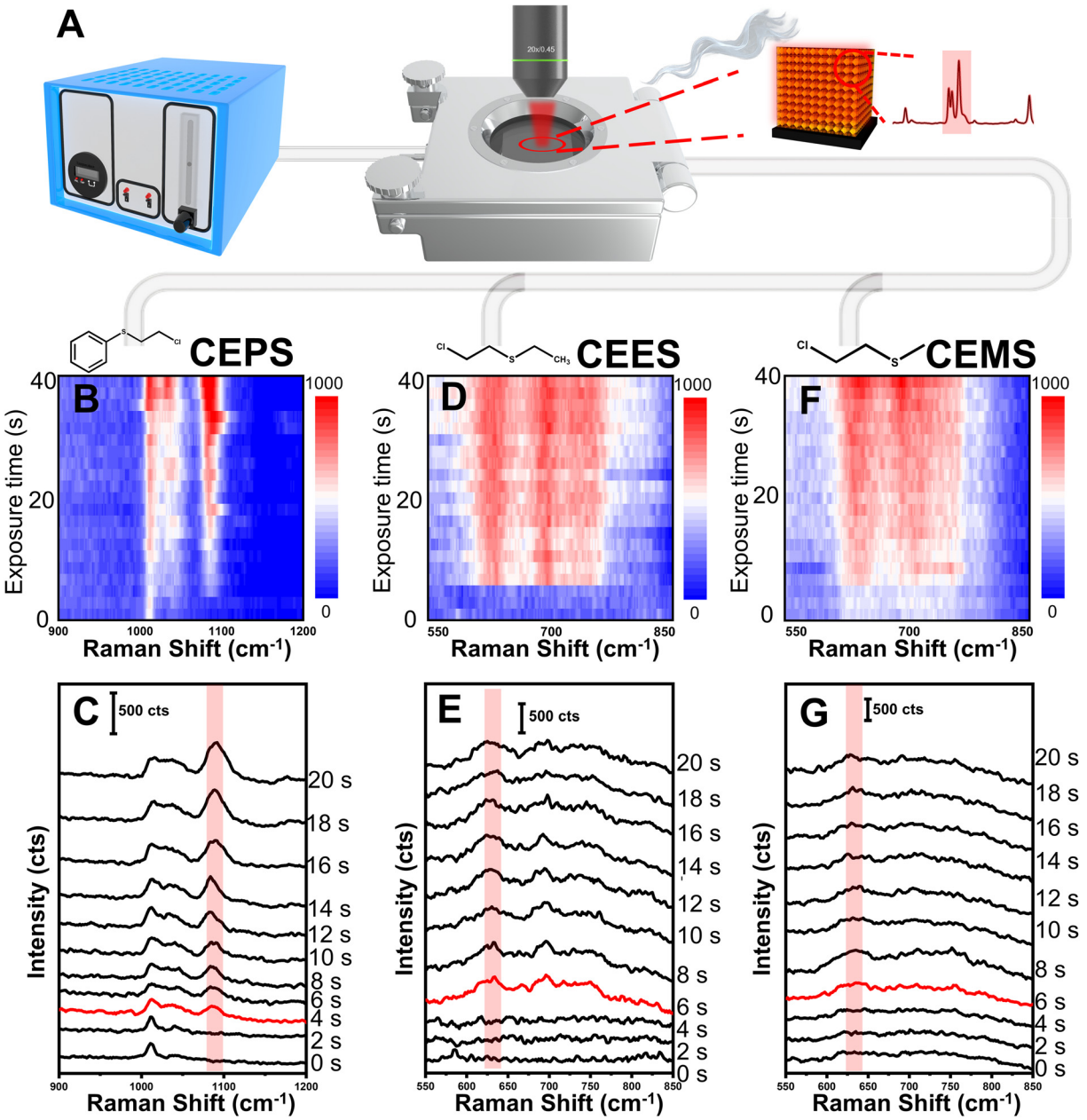

Fig. 7 Real-time SERS detection of gas-phase 2-CEPS, 2-CEES and 2-CEMS. (A) Schematic diagram of the setup for real-time SERS gas detection. Time-resolved heat maps constructed from SERS data and corresponding SERS spectra of (B and C) 2-CEPS (1 ppm); (D and E) 2-CEES (10 ppm) and (F and G) 2-CEMS (10 ppm) under a 785 nm laser.

cannot saturate the entire superstructure. Instead, only molecules adsorbing onto the outermost one or two nanoparticle assembly layers contributed dominantly to the signal. This critically highlighted the importance of superposition of surface charge accumulation existing in AOICS superstructures with intense electromagnetic field enhancement, which was confined precisely within the inter-gaps of these surface layers. Consequently, even the minimal, transient adsorption of analyte molecules in these accessible hot spots generates a strong, detectable SERS signal. This mechanism bypasses the slow diffusion required for bulk saturation, directly linking the ultrafast response to the exceptional near-field properties of our architecture. The detection limits (LODs) of AOICS superstructures were 0.5 ppm for 2-CEPS, and 10 ppm for both CEES and CEMS, whereas Au nanocube assemblies exhibited significantly higher LODs of 1, 100, and 100 ppm, respectively (Fig. S23–S25). These results highlight the critical role of charge-driven tip-to-tip hot spots in enhancing electromagnetic fields, which enables fast response times and lower detection limits. The findings provide a practical reference for the design of future high-performance Raman sensing platforms.

Conclusions

In this study, we successfully synthesized AOICSs *via* a two-step process involving Ag growth and galvanic replacement. This unique structure exhibited a distinctive near-field phenomenon, internal tip-induced surface charge accumulation, which was particularly pronounced in AOICSs with a cubic shell of 5 nm thickness. The mechanism facilitated localized charge accumulation at the center of the cubic shell surface, generating strong spSERS signals, which could not be achieved with conventional Au nanocubes. To further investigate the potential of this phenomenon, we performed dimer and trimer SERS measurements, which revealed the critical role of the structural degree of mismatch and contact surface area in modulating the above effect. Finite element method simulations confirmed that a low DM significantly enhanced the electric field. Based on these insights, we engineered a tip-to-tip superstructure assembly with a close-packing arrangement to minimize the DM value and maximize the superposition of surface charge accumulation through precise tip-to-tip alignment. The resulting AOICS substrate achieved an impressive SERS enhancement compared with Au nanocubes in the detection of three different analytes (2-NTT, R6G, and Thiram). Moreover, the enhanced surface charge accumulation effect resulted in an impressive LOD. The AOICS superstructures were further applied for real-time detection of CWA gases. For 1 ppm CEPS, a Raman signal was obtained within 4 s, which is seven times faster than Au nanocube superstructures (28 s). Moreover, Au nanocubes failed to produce detectable signals under 10 ppm CEES and CEMS, whereas AOICS superstructures generated clear signals within 6 s. These results confirm the superior enhancement capability of charge-driven tip-to-tip hot spots.

In conclusion, our findings introduce a plasmonic enhancement mechanism and provide a rational design strategy for optimizing tip-to-tip superposition in nanostructured assemblies. This work opens avenues for developing advanced sensing platforms with ultrasensitive detection capabilities.

Author contributions

Qiang Zhao and Sehyun Park contributed equally to this project; L. L. and S. P. supervised the research; all authors have given approval to the final version of the manuscript.

Conflicts of interest

The authors declare no competing financial interest.

Data availability

The data supporting this article have been included as part of the supplementary information (SI). Supplementary information: characterisation data and additional experimental and simulation data to complement the main manuscript. Fig. S1–S5 illustrate the formation mechanism and structural characterization of the Au-based nanostructures, including the galvanic replacement process under different Au^{3+} concentrations and the XRD spectra of intermediate and final products. Fig. S6–S9 present single-particle SERS measurements and numerical simulations for Au nanocubes, Au octahedra, and Au nanoshells. Fig. S10–S13 show the field enhancement and surface charge distributions of dimer and trimer assemblies under laser excitation, supported by FE-SEM images. Fig. S14–S18 demonstrate the formation, uniformity, and stability of Au nanocube and AOICSs superstructures. Fig. S19–S21 provide bulk SERS calibration and sensitivity analysis using different analytes (2-NTT, R6G, Thiram). Finally, Fig. S22–S25 highlight the real-time and quantitative gas-phase detection capabilities of the designed AOICS superstructures toward chemical warfare agent simulants (CEPS, CEES, CEMS). See DOI: https://doi.org/10.1039/d5nr04652a.

Acknowledgements

This work was supported by the National Research Foundation of Korea (NRF) grant funded by the Korean Government (MSIT) (NRF-2022R1A2C2002869 and RS-2024-00397807). This research was supported by the Challengeable Future Defense Technology Research and Development Program through the Agency for Defense Development (ADD) funded by the Defense Acquisition Program Administration (DAPA) in 2024 (915111201). This work was supported by the Yonsei Fellow Program funded by Lee Youn Jae. Q. Z. thanks the China Scholarship Council (no. 202308260024).

References

1 G. Li, X. Zhao, X. Tang, L. Yao, W. Li, J. Wang, X. Liu, B. Han, X. Fan, T. Qiu and Q. Hao, *Nano Lett.*, 2024, **24**, 13447–13454.
2 Y. Ma, K. Promthaveepong and N. Li, *ACS Sens.*, 2017, **2**, 135–139.
3 H. J. Park, S. Cho, M. Kim and Y. S. Jung, *Nano Lett.*, 2020, **20**, 2576–2584.
4 X. Wang, Y. Zhang, J. Yu, X. Xie, R. Deng, C. Min and X. Yuan, *ACS Nano*, 2022, **16**, 18621–18629.
5 G. Xu, J. Zhu, L. Song, W. Li, J. Tang, L. Cai and X. X. Han, *Nano Lett.*, 2024, **24**, 13843–13850.
6 H. Zhang, L. Yang, M. Zhang, H. Wei, L. Tong, H. Xu and Z. Li, *Nano Lett.*, 2024, **24**, 11116–11123.
7 J. Kim, H. Hilal, M. Haddadnezhad, J. Lee, W. Park, W. Park, J. W. Lee, I. Jung and S. Park, *ACS Nano*, 2022, **16**, 9214–9221.
8 S. Y. Lee, P. V. Tsalu, G. W. Kim, M. J. Seo, J. W. Hong and J. W. Ha, *Nano Lett.*, 2019, **19**, 2568–2574.

9 J. Shin, S. Lee, S. Yoo, I. Jung, S. Lee, J. Kim, J. Son, J.-E. Kim, J.-M. Kim, J.-M. Nam and S. Park, *Chem. Mater.*, 2022, **34**, 2197–2205.
10 X. Wang, L. Zhao, R. Zhao, Y. Zhou, S. Wang, X. Chi, Y. Xiong, Y. Yao, K. Zhang, Y. Li, Z. Yang and Y.-M. Yan, *Chem. Eng. J.*, 2022, **450**, 138316.
11 S. Yoo, S. Go, J. Son, J. Kim, S. Lee, M. Haddadnezhad, H. Hilal, J. M. Kim, J. M. Nam and S. Park, *J. Am. Chem. Soc.*, 2021, **143**, 15113–15119.
12 S. Yoo, J. Kim, S. Choi, D. Park and S. Park, *Nat. Commun.*, 2019, **10**, 5789.
13 A. Ten, V. Lomonosov, C. Boukouvala and E. Ringe, *ACS Nano*, 2024, **18**, 18785–18799.
14 C. Yuan, D. Zhang, P. Xu and Y. Gan, *ACS Appl. Nano Mater.*, 2024, **7**, 16141–16153.
15 J. Baril and A. Ianoul, *J. Phys. Chem. C*, 2024, **128**, 10880–10887.
16 A. Kaushik, J. Singh, R. Soni and J. P. Singh, *ACS Appl. Nano Mater.*, 2023, **6**, 9236–9246.
17 Y. Yao, J. Ji, H. Zhang, K. Zhang, B. Liu and P. Yang, *Anal. Chem.*, 2018, **90**, 10394–10399.
18 Y. Zhai, Y. Zheng, Z. Ma, Y. Cai, F. Wang, X. Guo, Y. Wen and H. Yang, *ACS Sens.*, 2019, **4**, 2958–2965.
19 X. Lin, P. Zhou, Q. Li and Y. Pang, *Anal. Chem.*, 2024, **96**, 10686–10695.
20 Z. Wang, L. Huang, M. Zhang, Z. Li, L. Wang, H. Jin, X. Mu and Z. Dai, *J. Am. Chem. Soc.*, 2022, **144**, 17330–17335.
21 J. Yu, C. Chen, Q. Zhang, J. Lin, X. Yang, L. Gu, H. Zhang, Z. Liu, Y. Wang, S. Zhang, X. Wang and L. Guo, *J. Am. Chem. Soc.*, 2022, **144**, 21908–21915.
22 S. Yoo, J. Lee, H. Hilal, I. Jung, W. Park, J. W. Lee, S. Choi and S. Park, *Nat. Commun.*, 2022, **13**, 4544.
23 Z. Zeng, X. Quan, H. Yu, S. Chen and S. Zhang, *J. Catal.*, 2019, **375**, 361–370.
24 Y. Zhao, Y. Yang, Y. Luo, X. Yang, M. Li and Q. Song, *ACS Appl. Mater. Interfaces*, 2015, **7**, 21780–21786.
25 P. Zheng, L. Wu and I. Barman, *J. Phys. Chem. C*, 2024, **128**, 14375–14380.
26 S. Kwon, H. Kim, Q. Zhao, M. J. Oh, K. Hur, I. Jung and S. Park, *Small*, 2025, **21**, e2410296.
27 S. Gómez-Graña, C. Fernández-López, L. Polavarapu, J.-B. Salmon, J. Leng, I. Pastoriza-Santos and J. Pérez-Juste, *Chem. Mater.*, 2015, **27**, 8310–8317.
28 T. Kang, J. Zhu, X. Luo, W. Jia, P. Wu and C. Cai, *Anal. Chem.*, 2021, **93**, 2519–2526.
29 J. Kim, Q. Zhao, I. Choi, M. J. Oh, S. Kwon and S. Park, *Nat. Commun.*, 2025, **16**, 2762.
30 M. Haddadnezhad, I. Jung, M. J. Oh and S. Park, *Adv. Mater.*, 2024, **36**, e2400068.
31 S. W. Chee, S. F. Tan, Z. Baraissov, M. Bosman and U. Mirsaidov, *Nat. Commun.*, 2017, **8**, 1224.
32 S. Lee, S. Lee, W. Park, S. Lee, S. Kwon, M. J. Oh, M. Haddadnezhad, I. Jung, B. Kim, J. Park, K. S. Shin, H. Lee, J. Yoo, W. K. Kim and S. Park, *Nano Lett.*, 2024, **24**, 4233–4240.